HOKKAIDO UNIVERSITY

Title	Preparation of highly active and durable electrodes for alkaline water electrolysis by anodizing of commercial FeNi and FeNiCo alloys
Author(s)	Zetao, Xiong; Quintero, David; Kitano, Sho et al.
Citation	Electrochimica acta, 491, 144352 https://doi.org/10.1016/j.electacta.2024.144352
Issue Date	2024-07-01
Doc URL	https://hdl.handle.net/2115/97213
Rights	© <2024>. This manuscript version is made available under the CC BY-NC-ND 4.0 license http://creativecommons.org/licenses/by-nc-nd/4.0/
Rights(URL)	https://creativecommons.org/licenses/by-nc-nd/4.0/
Type	journal article
File Information	Electrochim. Acta 491 144352 .pdf

Hokkaido University Collection of Scholarly and Academic Papers : HUSCAP

Preparation of highly active and durable electrodes for alkaline water electrolysis by anodizing of commercial FeNi and FeNiCo alloys

Xiong Zetao[1], David Quintero[2,*], Sho Kitano[2], Tomoya Nagao[1], Mana Iwai[2], Yoshitaka Aoki[2], Koji Fushimi[2], Hiroki Habazaki[2,*]

[1] Division of Applied Chemistry, Faculty of Engineering, Hokkaido University, Sapporo, Hokkaido 060-8628, Japan

[2] Graduate School of Chemical Sciences and Engineering, Hokkaido University, Sapporo, Hokkaido 060-8628, Japan

*e-mail: dalberto.quintero@eng.hokudai.ac.jp ; habazaki@eng.hokudai.ac.jp

Abstract

Anodizing is gaining popularity as a binder-free fabrication route for obtaining catalyst materials directly on the current collector without using noble metals, binders, or conductive carbon additives. Here, we fabricate promising highly active electrodes for alkaline water electrolysis by anodizing commercial FeNi and FeNiCo alloys (%wt. Fe range between 22 - 63) in an ethylene glycol-based fluoride electrolyte. Anodizing forms metal fluoride coatings, which are converted to OER active compounds (γ-NiOOH:Fe) during potential cycling in an alkaline aqueous solution (1 mol L^{-1} (M) KOH at 293 K) as a result of leaching of fluoride ions. The morphology, thickness, and number of active sites are

influenced by the amount of Fe in the alloy, and the electrode with the highest electrochemical active surface area (Kovar alloy with a 54 %wt. Fe) shows the largest OER activity enhancement by anodizing. The performance evaluation in practical conditions (7 mol L^{-1} KOH at 343 K) demonstrated a highly active performance with an OER potential as low as 1.52 V at a current density of 600 mA cm^{-2} even for electrodes obtained in alloys with a low amount of Fe (78-Permalloy with a 22 %wt. Fe), demonstrating that anodizing is an effective way to develop highly active OER electrodes from commercially available alloys. On the other hand, anodizing is a good fluoridation route for transition metals with good results in the formation of F-enriched precursors that efficiently promote active phase formation during the catalytic process, offering the possibility of obtaining catalysts directly on the current collector in a one-step process, easily implemented in industrial applications.

Keywords: Binder-free electrode, alkaline water electrolysis, FeNiCo alloys, OER/HER, anodizing.

1. Introduction

The depletion of oil resources and the environmental consequences of climate change, influenced by population growth, industrialization, and increased dependence on transportation means, have intensified the exploration of new energy solutions. Addressing these challenges demands transitioning to renewable sources, decreasing dependency on fossil fuels, and adopting cleaner technologies to reduce environmental degradation and confront climate change [1]. Hydrogen is considered a highly promising energy carrier; however, it qualifies as a green energy carrier only when its generation is free of greenhouse gas emissions (CO_2). Electrochemical water splitting is an environmentally friendly process

for obtaining green hydrogen [2,3]. However, the high cost of the H_2 produced by this method limits its extensive applicability, contributing only to ~4% of the total hydrogen production by 2020 [4]. The above is related to the low overall efficiency, which is restricted by the sluggish kinetics of the oxygen evolution reaction (OER), leading to a high overpotential and energy consumption [5,6]. However, considering various perspectives and future visions, the production of H_2 through water splitting needs to be increased by approximately 60% to accomplish the net-zero energy scenario goals by 2050 [7,8]; therefore, research in new materials or processes that exhibit greater efficiency using more cost-effective materials to enhance the sustainability of this technology is crucial.

Alkaline water electrolysis is the most established hydrogen generation electrochemical process, and it has been extensively used in industrial hydrogen production for decades [9,10]. The rising popularity of alkaline water electrolyzers is related to using of relatively inexpensive non-noble metals (Ni, Co and Fe). Among them, Ni-based catalysts show great potential for OER because of their high activity, good stability, and inexpensive cost [11,12]. In Ni-based materials, the formation of α-$Ni(OH)_2$ is observed as a main phase at the electrolyte-electrode interface, which can be oxidized by anodic polarization to obtain γ-NiOOH, widely known for its good OER activity. Trotochaud et al. [13] found that the good OER activity of the γ-NiOOH was related to the incorporation of Fe-impurities and the OER activity of the γ-NiOOH is low, and no significant OER current occurs until an overpotential > 400 mV when the material is evaluated in a Fe-free alkaline medium [14]. Therefore, the role of Fe in the OER activity of the γ-NiOOH has been an important research topic in recent years. The presence of Fe in the electrolyte or bulk materials promotes the formation of $Ni_{1-x}Fe_xOOH$, which is the most active catalyst measured in basic media [15–17]. Different

researchers have shown that the OER activity of the Ni-Fe catalysts depends on the amount of Fe, with a desirable Fe composition between 15% and 50%. In NiFe alloys with a Fe content above 60%, the γ-FeOOH formation is predominant, which is a compound with low OER activity. The OER overpotentials of good OER Ni-Fe catalysts are below <300 mV at a current density of 10 mA cm^{-2} [18–21], which are comparable to well-known materials that have good OER activity like IrO_2 (170 - 275 mV at 10 mA cm^{-2} [22,23]). Numerous experimental and theoretical investigations have recently been conducted to understand the role of iron (Fe) in enhancing the OER activity of γ-NiOOH, and a critical analysis is presented in this review [15]. The most crucial aspects of $Ni_{1-x}Fe_xOOH$ are that Fe is the active site in the catalysts [24], Fe enhances the electrical conductivity of NiOOH [13], the Fe-O bond in the $Ni_{1-x}Fe_xOOH$ catalysts has a ~7% contraction that enables more optimal adsorption energies for the intermediate species during O_2 release [25], in $Ni_{1-x}Fe_xOOH$ or γ-NiOOH, Fe^{+3} cations have much lower overpotential than Ni^{+3} ions [18] and the activation energy for Ni-Fe catalysts with a Fe composition between 20-40% is approximately 25-30 kJ mol^{-1}, a close value to the IrO_2 (15-16 kJ mol^{-1}), which is considered one of the most significant OER catalysts in terms of both activity and stability [26]. On the other hand, the Co addition to the Ni oxide films does not appear to enhance OER activity, but in the NiFeCo catalyst, Co and Fe have a synergistic effect, enhancing the OER activity of $Ni_{1-x}Fe_xOOH$ while not affecting γ-NiOOH, contributing to increasing interest in NiFeCo catalysts [20,27,28].

The chemical composition of the electrodes is an essential factor in obtaining a good OER catalyst; however, the durability and stability over time are highly affected by the electrode configuration. Binder-free electrodes are a new strategy characterized for the direct

deposition or formation of the catalysts on the current collector, avoiding the use of carbon conducting aids and binders, with some advantages such as an increased density of exposed active sites, a rapid mass transport, electrolyte penetration, and minimal contact resistance. The most common methods are electrodeposition, electroless deposition and chemical vapor deposition [29–35]. Furthermore, several strategies for improving catalytic performance have been widely studied, such as increasing the specific surface area and controlling the chemical composition by alloying, doping and in-situ electrochemical activation [36]. Fluoridation has recently been identified as an important strategy for improving the performance of OER catalysts considering its effect on structure transformation, easy production and the exposure of active phases. F-enriched NiFe hydroxide is a promising precursor for developing highly active OER electrodes, given that oxidation by potential cycling or polarization produces OER active species like γ-NiOOH:Fe, and the measured activities exhibit a good performance regardless of the synthesis method [25,37,38]. Yamada et al. [19] obtained NiFe coatings with at.%Fe between 7.2 and 21.1 by electrodeposition. The subsequent anodization in a fluoride-containing organic solution exhibited outstanding OER performance for the anodized Ni-11.8 at.%Fe coating with an OER overpotential of 260 mV at 10 mA cm^{-2}. Fan et al. [39] anodized a NiFeCo alloy in a fluoride-containing organic solution, with an overpotential for OER of 170 mV at a current density of 5 mA cm^{-2}. Nishimoto et al. [40] anodized a bulk Ni-54 %wt.Fe-16.3 %wt.Co alloy for 250 s in a fluoride-containing organic solution, demonstrating the low OER overpotential of 260 mV at 10 mA cm^{-2}. Additionally, the results emphasize that the anodized material performs better than the non-anodized material. Pei et al. [25] prepared fluoridated FeNi-LDHs by using ammonium fluoride with post heat treatment at 250 ˚C and showed an OER overpotential of 225 mV at 10 mA cm^{-2}

as the most outstanding performance. From the above results, it is important to note that the anodizing process is gaining popularity as a promising route for fabricating F-enriched binder-free OER electrodes. The direct formation of Ni hydroxide from the substrate avoids intermediate steps such as electrodeposition, porous coatings with a high surface area can be obtained and the amorphous nature of the anodic coating is crucial to guarantee the optimal conditions of OER catalysts ($Ni_{1-x}Fe_xOOH$ or γ-NiOOH) [19,40,41]. While electrodeposited-anodized layers of NiFe and anodized FeNiCo alloys have been investigated, additional research to understand the effect of the composition of commercial FeNi and FeNiCo alloys on the formation of F-enriched Ni oxyhydroxide compounds obtained by anodizing and their OER performance is needed. Furthermore, most of the research has been focused on testing OER activity at low temperatures and low KOH concentrations; therefore, understanding the OER performance of anodized electrodes under practical conditions as obtained in an alkaline electrolyzer is crucial. In this study, NiFe and NiFeCo alloys, with Fe contents between 22.2 to 63 %wt, were anodized in a fluoride-containing organic electrolyte, and the OER activity was evaluated under practical alkaline electrolyzer conditions (7 M KOH at 343 K). The commercial alloys showed a surface morphology and electrochemical surface area strongly dependent on the amount of Fe in the alloy in 1 M KOH at 293 K. Overall, the results of this study demonstrate that the anodized FeNi and FeNiCo alloys are promising candidates as electrocatalysts for OER reactions. The evaluation of the electrodes in practical conditions (7 M KOH at 343 K) evidenced a highly active performance with an overall potential as low as 1.52 V at a current density of 600 mA cm^{-2}. The best HER performance was observed for pure Ni and reduced with a higher amount of Fe in the alloy.

2. Experimental

2.1. *Preparation of the electrodes for alkaline water electrolysis:* FeNi and FeNiCo commercial alloys (78-Permalloy, 45-Permalloy, Kovar, 42-Invar, Super invar) were used for the preparation of the electrodes for alkaline water electrolysis. The chemical composition of the alloys is summarized in Table 1. Plates with dimensions of 1.2 × 2.5 × 0.2 cm were cut and washed ultrasonically with acetone and Milli-Q water. An area of 1.44 cm^2 was demarcated using a PTFE film-based adhesive tape (Nitto Denko, P-422 NAT)(See Fig.S1). The anodizing process was carried out at 10 V for 60 min in an ethylene glycol-based electrolyte containing 0.54 M NH_4F and 2.5 M H_2O, employing a KIKUSUI PAS500 - 0.6 power supply connected to an Agilent 34460A multimeter for data recording. A two-electrode cell configuration made of a PTFE was used, using 100 mL of electrolyte with platinum as a counter electrode, keeping the temperature constant at 293 K using a temperature controller unit (Multi-Thermal Unit TMi - 150). During the anodization, the electrolyte was not stirred, and the distance between the electrodes was ~ 2 cm. After anodizing, samples were washed with Milli-Q water and dried with a cool air stream.

Table 1. Composition of the FeNi and FeNiCo commercial alloys

Material	Fe (%wt.)	Ni (% wt.)	Co (% wt.)
78-Permalloy	22.2	77.8	--
45-Permalloy	54.4	45.6	--
Kovar	54.0	29.7	16.3
42-Invar	59.1	40.9	--

Super invar	63.0	32.0	5.0

2.2. *Preparation of electrodes with high Ni content:* The formation of anodic coatings in high-Ni-content alloys shows a low growth rate (as shown later in Figure 2) with a low incorporation of F from the electrolyte. Therefore, an extra anodizing process at 50 V for 60 min in an ethylene glycol-based electrolyte containing 0.08 M NH_4F and 0.02 M H_2O was performed in the 78-permalloy and pure Ni. The anodizing process was carried out under the same conditions described in section 2.1.

2.3. *Compositional and morphology characterization***:** The surface and cross-section observations were assessed by a field-emission scanning electron microscope (ZEISS, Sigma-500) operated at 1 kV equipped with energy-dispersive X-ray spectroscopy (EDS, Bruker, Quantex). EDS elemental analysis was performed by applying an acceleration voltage of 3 kV. For the cross-section observations, the anodized sample was embedded in epoxy resin (Epoxy (G2), JEOL), and the cross-section was prepared by a broad ion milling technique (JEOL, IB-19530CP). Phases in the electrodes were identified by X-ray diffraction (XRD) utilizing Cu K_α radiation ($\lambda = 0.15418$ nm), applying 40 kV and 20 mA. Herein, α-2θ mode measurements, where $\alpha = 2°$, were used to enhance the reflections from the porous surface layer. Phases in the anodized electrodes before and after immersion or polarization in the KOH electrolyte were also identified by Raman spectroscopy measurements (Horiba Scientific, XploRA) using a 532-nm laser beam.

2.4. *OER Performance:* The OER performance was assessed by cyclic voltammetry (CV) using a Versa STAT4 potentiostat in a three-electrode electrochemical cell composed of the prepared electrode as a working electrode, a platinum plate as a counter-electrode, and a 1M KOH/Hg/HgO as a reference electrode (See Fig. S2). The cell was a 100 ml beaker made of PTFE. The measurements were conducted in a 1 M KOH solution (Purity ≥ 86% and Fe content of max. 5 ppm) at 293 K. The exposed area was 1.44 cm^2 and was demarcated using a PTFE film-based adhesive tape (Nitto Denko, P-422 NAT). The CV sweep range was between 1.1 to 1.6 V vs. reversible hydrogen electrode (RHE) for the anodized samples and between 1.1 to 1.7 V vs. RHE for the as-received samples with a sweep rate of 10 mV s^{-1}. The potentials were converted to RHE for the CV analysis. The iR correction was performed by subtracting the solution resistance (Tables S1-S2) and current product from the measured potential. Electrochemical impedance spectroscopy (EIS) was assessed after the potential cycling at 1.5 V vs. RHE for OER in a stagnant 1 M KOH solution at 293 K, in a frequency range from 1 MHz to 0.1 Hz, and an amplitude of 10 mV. The electrochemical parameters were evaluated by fitting the EIS experimental results using the equivalent circuit and the methodology reported in a previous study [42] (See Figs. S3-S4).

2.5. *Electrochemical active surface area (ECSA):* ECSA was assessed in the as-received and anodized electrodes based on previous studies [43,44]. For ECSA estimation, CV measurements were conducted in the potential range of 0.7 ~ 0.8 V vs. RHE, where no charge-transfer reaction occurs. The sweep rates were 10, 20, 40, 80 and 100 mV s^{-1} (Figs. S5-S6), and the electric double-layer capacitance (C_{dl}) of each sample was then calculated using the following equation (1).

$$i_a = vC_{dl} \qquad (1)$$

where v is the sweep rate and i_a is the current density.

Once the measurements were completed, the relationship between the current and sweep rate at 0.75 V was plotted. Linear relationships were obtained for each alloy and C_{dl} was estimated from the slope. The graphs are shown in Figs. S7-S8, and results are summarized in Table 3.

2.6. *Performance of the electrodes prepared at practical alkaline electrolyzer condition:* OER/HER activity was assessed on the anodized electrodes at 343 K by CV in a 7 M KOH solution (Purity ≥ 86% and Fe content of max. 5 ppm). The exposed area was 1.44 cm^2 and was demarcated using a PTFE film-based adhesive tape (Nitto Denko, P-422 NAT). The cell was a 300 mL beaker made of PTFE. The CV sweep range was 1.1 ~ 1.7 V vs. RHE for the OER and 0 ~ -0.6V vs. RHE for HER, and the sweep rate was 10 mV s^{-1}. Durability experiments under practical electrolysis conditions were performed in the electrodes prepared on the 78-Permalloy, Kovar, and 42-Invar alloys, applying a current density of 600 mA cm^{-2} in a 7M KOH solution at 343 K for 80 h. Durability tests were assessed using a BioLogic, Model VSP Potentiostat, in a thermostatic oven using a three-electrode electrochemical configuration designed to keep the temperature and electrode distance stable (Fig. S9). The three-electrode system is composed of the prepared electrode as the working electrode, a platinum plate as a counter electrode, and a hydrogen electrode (EDAQ, Model ET070) as a reference electrode.

3. Results and Discussion

3.1. *Characterization of the anodic films obtained on FeNi and FeNiCo alloys:* Figure 1 shows the current transients recorded during anodizing at 10 V in ethylene glycol containing 0.54 M NH_4F and 2.5 M H_2O. At the commencement of anodizing, the current increases to a maximum value because of the application of a high electric field to a thin air-formed oxide film on the alloys. Then, the current decreases sharply due to the thickening of a compact anodic coating, with a subsequent steady-state current stage, which reflects the balance of coating formation at the alloy-coating interface and the field-assisted dissolution at the coating-electrolyte interface [45,46]. Two different patterns during the steady-state current are observed during the anodizing process of the FeNi and FeNiCo alloys. The 78-permalloy and Super Invar materials have current transients that are stable until the end of the process, with the lowest current density for the 78-permalloy (Fig. 1a-b). A low current density during anodizing at constant potential reflects the formation of a thin oxide layer of a uniform thickness [47]. In the alloys with %wt. Fe between 54-59, a two-stage steady-state current density is observed. First, the current density increases until it reaches a higher steady-state value. The highest current density at the end of the anodizing process is for the Kovar alloy (Fig. 1b). The two stages in the steady-state current are generated by the local thickening of the oxide layer as a result of the local breakdown of a barrier layer [46,48].

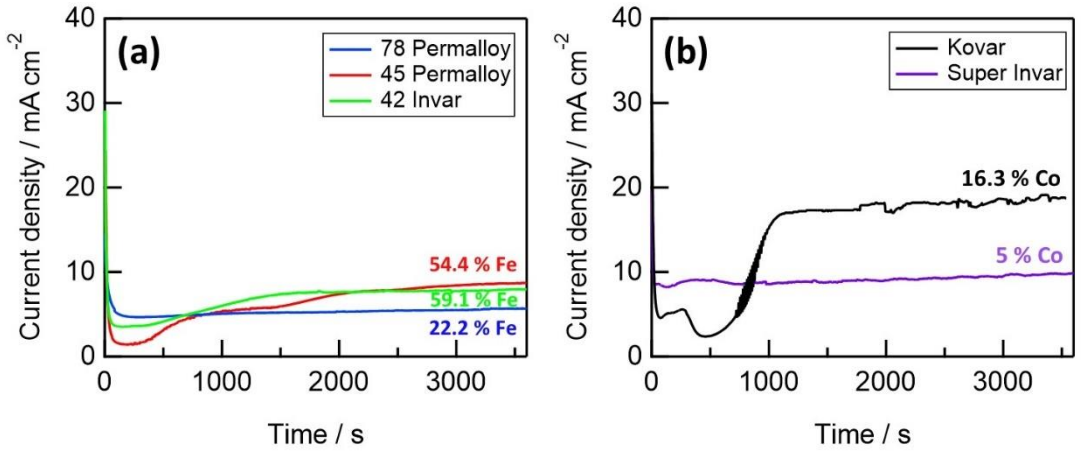


Figure 1. Current transients during the anodizing process of the (a) FeNi and (b) FeNiCo alloys at 10 V in ethylene glycol containing 0.54 M NH_4F and 2.5 M H_2O.

The surface and cross-section morphologies of the anodic coatings were assessed by SEM, as shown in Fig. 2. The surface morphology strongly depends on the amount of Fe in the FeNi and FeNiCo alloys. For the 78-Permalloy and Super Invar, a coating with homogenous thickness is evidenced with thicknesses of ~100 nm and ~1.5 µm, respectively (Figs. 2b and 2j). The thin coating of the 78-permalloy has low porosity (see Fig. S10), and the grain boundaries of the alloy substrate remain visible even after anodization. The Super Invar alloy containing both Fe and Co increases the current; as a result, a thicker coating is obtained (Fig. 2j). A homogeneous coating thickness formation is characteristic of a current transient stable with a coating thickness dependent on the current density value (Fig. 1) [48]. In the alloys with Fe content of 54-59 %wt., a craquelure morphology was observed with a variation in its distribution based on the alloying elements. 45-Permalloy (Fig. 2c) and 42-Invar (Fig. 2g) alloys show a similar morphology with thin cracks and a non-uniform coating with an average thickness of ~ 1 µm (Figs. 2 d, h). The Kovar alloy (Fig. 2e) shows the

formation of wide cracks and non-uniform coating with a thickness of ~ 1.8 μm. The higher thickness coating is due to the higher current density during anodizing, contributing to forming a thicker coating (Fig. 2f) [49]. In the 45-Permalloy, Kovar and 42-Invar alloys, the coating-substrate interface has a scalloped morphology edge, and the morphology reflects the local thickening of the oxide during the anodizing process, which is characteristic of the two-stage steady-state current density (Fig. 1). Nishimoto et al. [46] anodized the Kovar alloy at different temperatures, emphasizing that a steady-state current with a stable behavior conducts the formation of homogenous coating with a smoothness interface between the metal-oxide (anodization at 30 and 40 ˚C), while a variable steady-state current promotes the formation of coating with a non-homogenous thickness (anodization at 10 - 20 ˚C), similar to the anodization of FeNi and FeNiCo alloys.

The composition and phase formation of the anodic coatings were assessed by XRD (Fig. 3), EDS (Table 2) and Raman spectroscopy (Fig. S11a). EDS analysis evidences the presence of fluorine species incorporated from the electrolyte, in agreement with the literature [11,50], with the presence of oxygen species in minor proportion. Metal fluoride ($(NiFe)F_2$) is the main crystalline phase observed after anodizing (ICSD 98-000-9168 and ICSD 98-000-9166) (See Fig. 3a), in agreement with previous reports [40,46]. No visible peaks are present in the 78-permalloy material, which could be related to the formation of an amorphous phase and/or a thin layer formation, which are not usually detected by XRD [51]. XRD patterns of anodic coatings contain always the reflections from alloy substrates (Fig. 3b) because of the limited thickness of the anodic coatings. Raman spectra of the anodic coatings do not show characteristic peaks (Fig. S11a), which could be related to the low Raman scattering of the crystalline fluoride precursors [52,53].

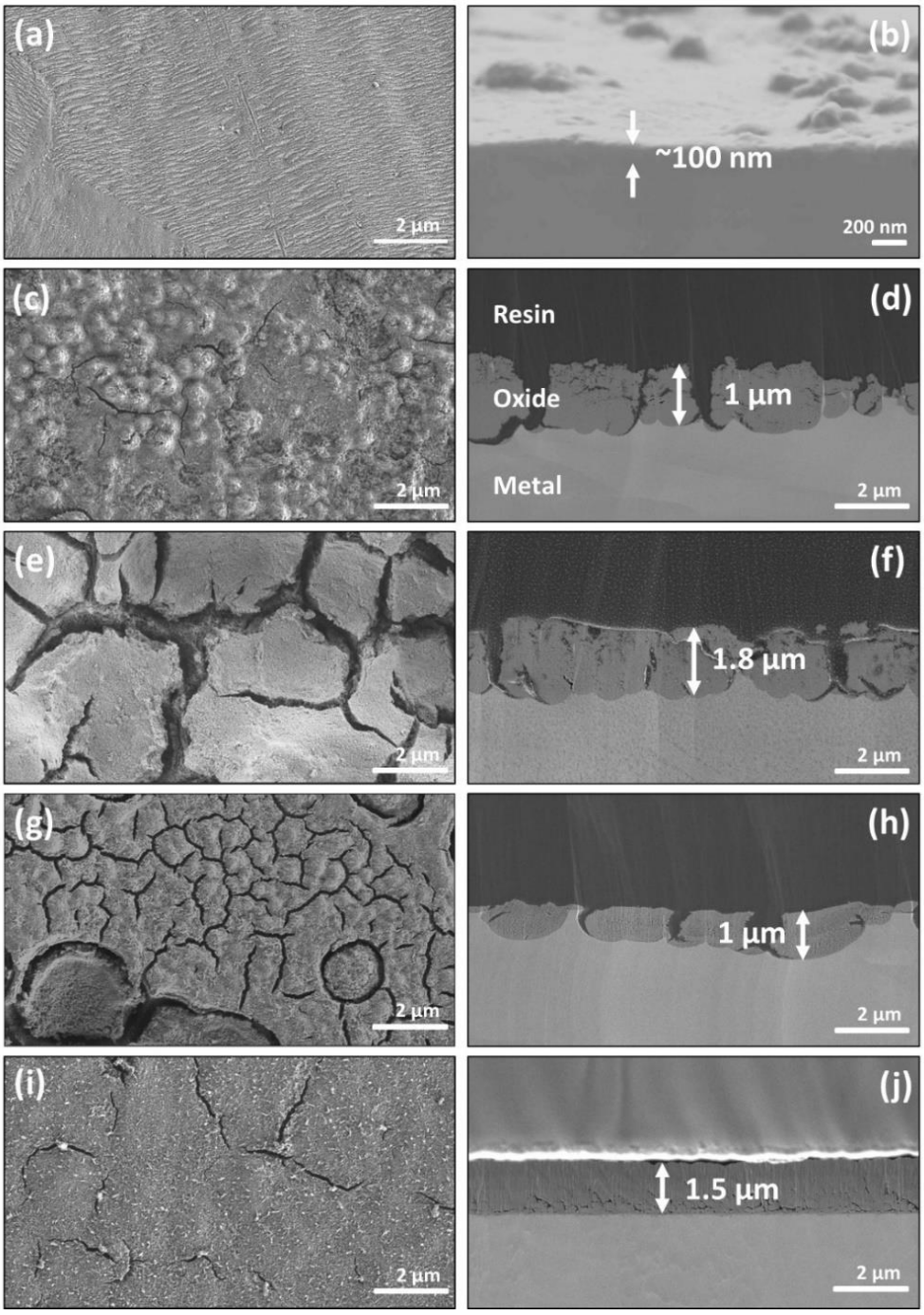


Figure 2. Surface SEM images (a, c, e, g, i) and cross-section SEM images (b, d, f, h, j) of the anodic coatings obtained at 10 V in ethylene glycol containing 0.54 M NH_4F and 2.5 M H_2O in (a, b) 78-Permalloy, (c, d) 45-Permalloy, (e, f) Kovar, (g, h) 42-Invar and (i, j) Super Invar.

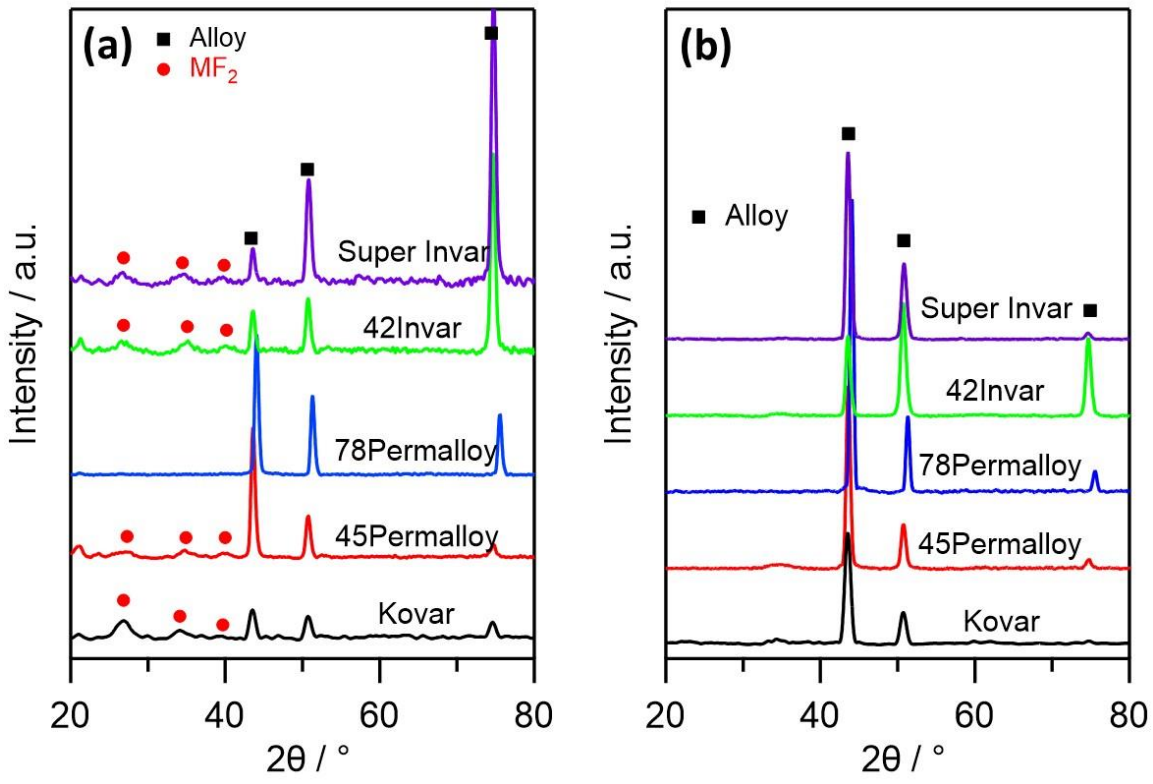


Figure 3. XRD patterns of the FeNi and FeNiCo alloys in the (a) as-anodized and (b) as-received conditions. The anodizing process was carried out at 10 V in ethylene glycol containing 0.54 M NH_4F and 2.5 M H_2O.

Table 2. Elemental composition assessed by EDS of the anodic coatings obtained on the FeNi and FeNiCo alloys and the elemental composition variation after OER evaluation.

Alloy	Anodizing potential	OER Evaluation	% Atm assessed by EDS				
			O	F	Fe	Co	Ni
Ni[1]	50 V	Anodized	5.4	25.1	-	-	69.5
		1 M KOH at 293 K	34.2	0.0	-	-	65.8
		7 M KOH at 343 K	30.7	0.0	-	-	69.3
78Permalloy[2]	10 V	Anodized	5.7	28.1	12.8	-	53.4
		1 M KOH at 293 K	50.2	0.9	10.2	-	38.7

78Permalloy[1]	50 V	Anodized	4.7	55.9	15.9	-	23.5
		1 M KOH at 293 K	71.7	0.0	5.9	-	22.4
		7 M KOH at 343 K	71.3	0.0	1.9	-	26.8
45Permalloy[2]	10 V	Anodized	11.4	45.7	28.4	-	14.5
		1 M KOH at 293 K	68.7	0.0	14.9	-	16.4
		7 M KOH at 343 K	66.5	0.0	8.1	-	25.4
Kovar[2]	10 V	Anodized	10.2	49.9	29.6	1.1	9.2
		1 M KOH at 293 K	73.4	0.0	11.2	2.4	13.0
		7 M KOH at 343 K	69.1	0.0	11.3	3.5	16.1
42Invar[2]	10 V	Anodized	12.4	38.5	29.9	-	19.2
		1 M KOH at 293 K	67.8	0.0	16.8	-	14.9
		7 M KOH at 343 K	52.5	0.0	13.9	-	33.6
Super Invar[2]	10 V	Anodized	14.8	37.1	31.6	1.8	14.7
		1 M KOH at 293 K	70.1	0.0	16.7	0.4	12.8
		7 M KOH at 343 K	54.5	0.0	16.7	0.3	28.5

[1] The anodizing solution is ethylene glycol containing 0.08 M NH_4F and 0.02 M H_2O.

[2] The anodizing solution is ethylene glycol containing 0.54 M NH_4F and 2.5 M H_2O.

3.2. *OER Characteristics:* OER performance was assessed by potential cycling in a 1 M KOH solution at 293 K. The potential cycling was performed during 15 cycles, and the last cycle is shown in Fig. 4. The potential cycling of NiFe and NiFeCo alloys differs in their Ni^{+2}/Ni^{+3} redox peak. From the CV curves of the alloys in the as-received condition, the redox peak is visible in the pure Ni, but in NiFe and NiFeCo alloys, the Ni^{+2}/Ni^{+3} peak is absent. The presence of Fe suppresses or shifts the redox peak to higher potential, as is well-known in the literature [54,55]. After anodizing, the Ni^{+2}/Ni^{+3} peak is observed in the 78-permalloy, whereas in the alloys with a higher amount of Fe (45-permalloy and 42-invar), the Ni^{+2}/Ni^{+3}

peak shifts to higher potentials, generating a kinetic competition between the metal oxidation process and metal reduction during O_2 release. The presence of Co in FeNiCo alloys shifts the Ni^{+2}/Ni^{+3} peak to negative values, as is evidenced in CV curves, showing a higher peak area, the alloy with a greater amount of Co (Kovar). The OER performance is summarized in Figure 4 and Table 3. Comparing the overpotential at a specific current density is a practical technique for assessing the OER activity of electrodes; in particular, the overpotential required to achieve a current density of 10 mA cm^{-2} is a widely adopted parameter to evaluate the OER activities [56]. In the as-received electrodes, Kovar shows the best OER activity with an overpotential of 324 mV, whereas pure Ni has the lowest OER activity with an overpotential of 364 mV, a value in agreement with literature reports [21]. The Fe addition reduces the OER overpotential in a range between 20 - 40 mV regarding pure Ni, without a clear pattern regarding the amount of iron in the alloy. Anodizing of alloys activates the material surface, making an important contribution to enhancing the OER activity of the FeNi and FeNiCo alloys, which is especially visible for the alloys with %wt. Fe between 54 and 59, with a reduction in the OER overpotential between 110-126 mV regarding pure Ni (see Table 3). The best OER performance among the anodized alloys is for the Kovar alloy, which has an OER overpotential of 239 mV at 10 mA cm^{-2}. The current density standardized by ECSA at 1.53 V vs HER enables the comparison of the OER performances of the coatings per active site, where a good correlation is observed between the OER overpotential (Fig. 5a) and the standardized current by ECSA (Fig. 5b), indicating that the most OER active sites are generated on Kovar by anodizing. Thus, the chemical composition of the active species plays one of the important roles in enhancing the OER activity. The ECSA shown in Table 3 discloses that anodizing the alloys increases the ECSA

with the highest value again for Kovar. The formation of the thickest coating on Kovar by anodizing may be one of the crucial contributions to enhancing the ECSA. A similar tendency was observed between the electric double-layer capacitance C_{dl} and the OER activity; the higher the electric double-layer capacitance, the better the OER activity (See Table S2). A good agreement between the non-Faradaic C_{dl} and EIS parameters allows reliable conclusions in agreement with the literature [57].

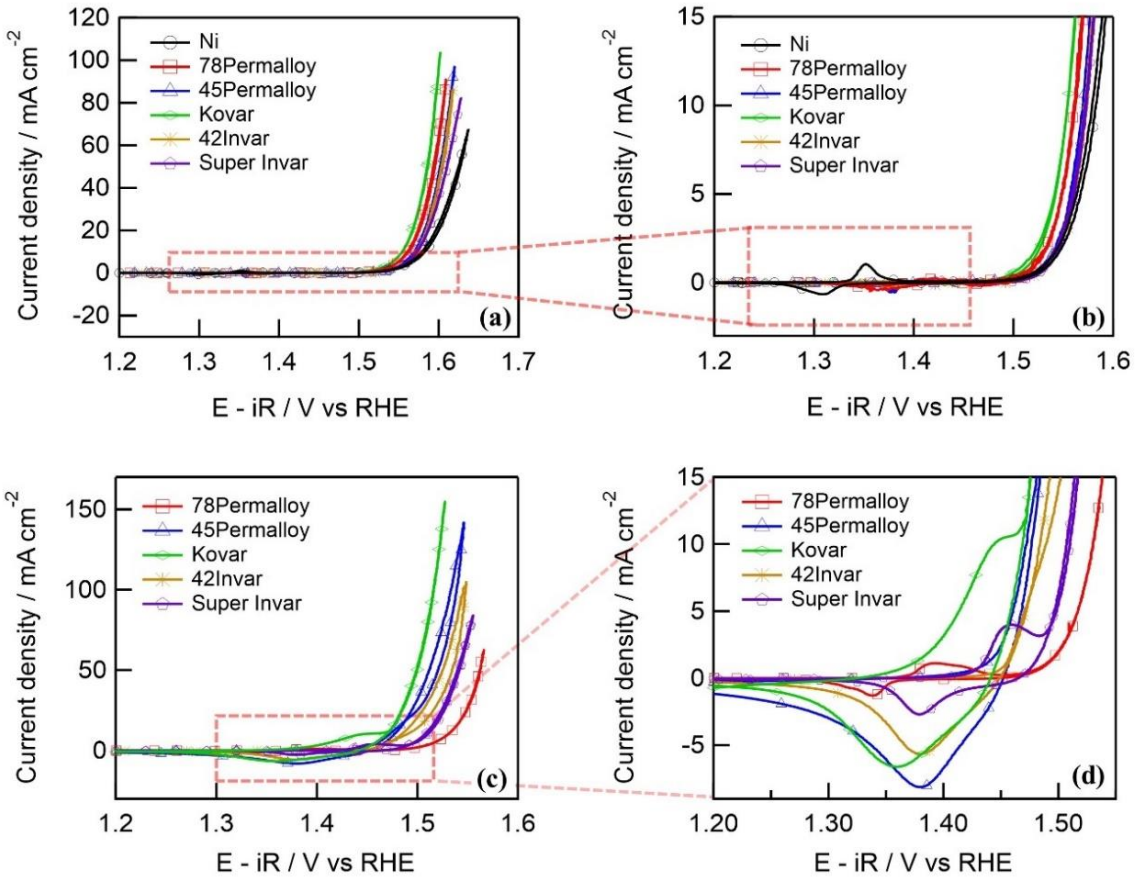


Figure 4. Last CV cycle in a 1M KOH solution on the FeNi and FeNiCo alloys in the (a, b) as-received condition and (c, d) after anodizing at 10 V in ethylene glycol containing 0.54M NH_4F and 2.5M H_2O. The record of the CV Curves during the 15 cycles is shown in Figure S12.

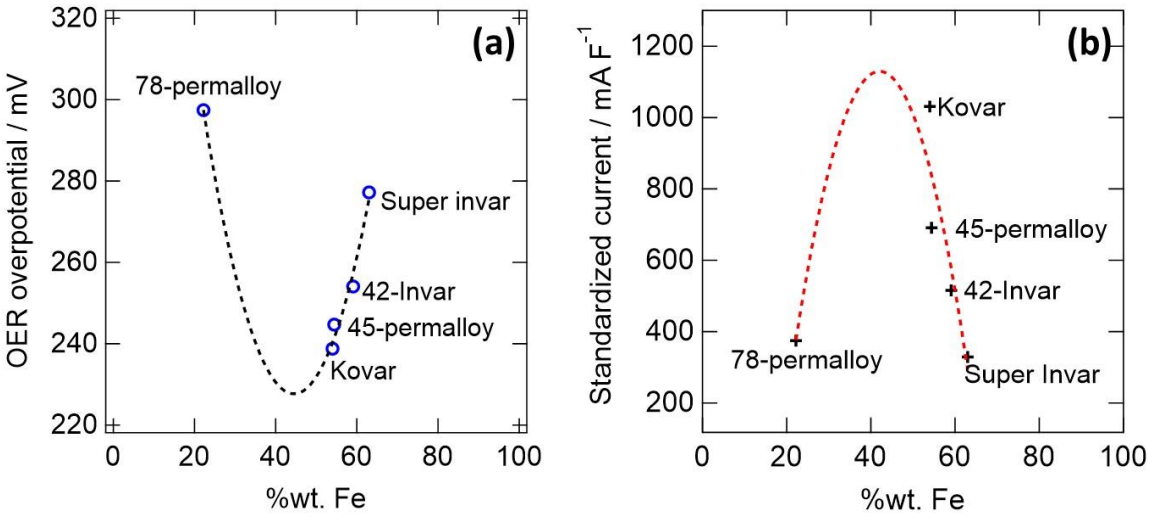


Figure 5. (a) OER overpotential (mV) and (b) standardized current by ECSA (mA F^{-1}) vs the amount of (%wt.) Fe in the FeNi and FeNiCo alloys for the anodized electrodes at 10V in ethylene glycol containing 0.54 M NH_4F and 2.5 M H_2O.

The EDS analysis (Table 2) shows that the fluoride ions in the coating are completely dissolved after the OER evaluation in 1 M KOH. Therefore, the increased ECSA after the OER evaluation in an alkaline media is due to the leaching of the fluoride ions, which generates the active oxyhydroxide species in agreement with the literature reports [19,25,36,40,46]. XRD patterns show that non-crystalline phases are present after OER activation (Fig. S11b). The Raman spectroscopy reveals the formation of the ɣ-NiOOH phase in the anodic coatings (corresponding peaks are 474 cm^{-1} and 554 cm^{-1}) and an additional shoulder peak appears at 685 cm^{-1}, which could be associated with the presence of iron oxide or hydroxide (Fe_3O_4, FeO or FeOOH) [58,59]. The formation of γ-FeOOH is well-known in the FeNi alloys whose proportion depends on the Fe content [18]. In the ɣ-NiOOH phase, the intensity of the 474 cm^{-1} band is higher than the 554 cm^{-1} band, nevertheless, the increased

intensity of the 554 cm^{-1} band (see Fig. 6) indicates that the ɣ-NiOOH is Fe-doped, which results in the formation of the $Ni_{1-x}Fe_xOOH$ phase [20,40]. The absence of the characteristic peaks in the 78-Permalloy could be related to the formation of a thin coating. Previous reports indicate that a fluoride coating formed by anodizing Kovar in a fluoride-containing ethylene glycol electrolyte is converted to a highly OER active FeNiCo oxyhydroxide during OER in KOH electrolyte [40,46]. The formation of the oxyhydroxide layer with a high ECSA highly enhances the OER activity. This study demonstrates that the OER active oxyhydroxide layers are formed by anodizing FeNi alloys and subsequent anodic polarization in KOH electrolyte. The transformation of fluoride to oxyhydroxide did not cause a significant change in the surface morphology, as can be confirmed by the comparison between Fig. 2 and Fig. S13. This transformation may be associated with the poor chemical stability of FeNi fluoride in KOH electrolyte; the fluoride may be attached by OH^- ions, resulting in the release of F^- ions into the electrolyte and the formation of oxyhydroxide. The detailed conversion process is under investigation. The Tafel slope relates to the rate-determining step of OER. In the as-received alloy electrodes, the alloying elements (Fe and Co) reduce the Tafel slope of the FeNi and FeNiCo alloys compared to Ni, since heteroatoms can modify the surface adsorption/desorption energy of intermediate species [60]. In the anodized electrodes, especially the alloys with %wt. Fe between 54-59, the Tafel slope is reduced to ~40 mV $decade^{-1}$, which suggests that the overall rate of the OER of the anodized materials is determined by the intermediate steps (Reaction R2 in Table S3) of the oxygen evolution reaction process, in agreement with a previous report [40].

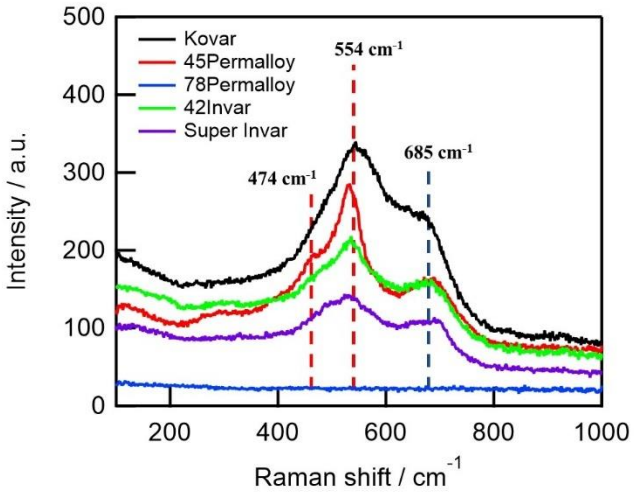


Figure 6. Raman spectrum of the anodic coatings obtained at 10 V in ethylene glycol containing 0.54M NH_4F and 2.5M H_2O after OER evaluation in 1M KOH at 293 K.

From the OER activity tendency against the %wt. Fe content in the alloy, the highest activity is expected in the region of Fe content between 35 and 45 wt.% (Fig. 5), consistent with previous studies [13,18,20,26]. In our research, FeNi alloys with Fe contents between 35-45 %wt. were not evaluated, but the OER overpotential obtained in the alloys with Fe content between 54 and 59 %wt. is comparable to or lower than FeNi catalyst with the optimal Fe content (See Table 4). Thus, porous fluoride coatings formed by anodizing FeNiCo alloys are promising precursors to form OER-active FeNiCo oxyhydroxide coatings with high surface area and specific OER activity. Table 4 compares the results obtained in our research with other FeNi alloys with different %wt. Fe, in which it is clear that the Fe has an important effect on the OER performance; nonetheless, when an in-situ activation or doping process is performed, the OER activity of alloys out of the optimal Fe range can be improved, as is evidenced in this study and by other authors [61]. In addition, anodizing is a well-known technique that has been used in the industry for decades [62] and outperforms

other treatment methods that require a long time or high temperatures, which restricts its use in the industry [63–65].

Table 3. Electrochemical characteristics of the anodic coatings obtained at 10V in ethylene glycol containing 0.54 M NH_4F and 2.5 M H_2O after OER evaluation in 1M KOH at 293 K.

Condition	Alloy	Overpotential[1] (mV)	Tafel slope (mV/decade)	ECSA (mF/cm^2)	Standardized[2] Current (mA/F)
As received	Ni	364	71	22	21
	78 Permalloy	332	54	23	81
	45 Permalloy	341	61	19	53
	Kovar	324	51	20	120
	42 Invar	344	63	19	47
	Super Invar	343	65	25	28
Anodized	78 Permalloy	297	59	23	418
	45 Permalloy	245	41	123	731
	Kovar	239	40	152	1020
	42 Invar	254	41	112	522
	Super Invar	277	56	87	344

[1] The OER overpotential was estimated at a current density of 10 mA cm^{-2} in the reverse sweep of the CV curves.

[2] Standardization of the current of OER at 1.53 V vs RHE.

Table 4. Overpotential and Tafel Slope comparison of FeNi electrocatalysts in 1.0 M KOH Electrolyte.

Material	Fe content	Coating formation or activation process	Tafel slope (mV/ decade)	OER Overpotential (mV)	Reference
Ni	--	Electrodeposited Ni	72	371 at 10 mA cm^{-2}	[21]

FeNi	11.8 %atm.	Electrodeposited FeNi and anodizing in fluoride-containing solution		260 at 10 mA cm^{-2}	[19]
FeNi	10 %atm.	Electrodeposited FeNi film	65	375 at 10 mA cm^{-2}	[26]
FeNi	25 %atm.	Electrodeposited FeNi film	40	375 at 10 mA cm^{-2}	[18]
78-Permalloy	24 %wt.	Anodizing in fluoride-containing solution	59	297 at 10 mA cm^{-2}	In this work
FeNi	31% atm.	Carbon-Supported Ni–Fe Nanoparticles	30	280 at 10 mA cm^{-2}	[66]
Ni_8Fe_2 alloy	--	Powder Metallurgy	42.5	269 at 10 mA cm^{-2}	[64]
FeNi hydroxide	FeNi 1:2	FeNi 1:2 electrodeposited on Ni by 600 s	30	200 at 10 mA cm^{-2}	[67]
FeNi	35 %atm.	Electrodeposited FeNi film	60	330 at 10 mA cm^{-2}	[26]
FeNi		Composite of carbon fibers and FeNi alloy	49	317 at 10 mA cm^{-2}	[68]
Kovar	54 %wt.	Anodizing in fluoride-containing solution	40	239 at 10 mA cm^{-2}	In this work
FeNi	67 %wt.	Electrodeposited FeNi film	~40	320 at 10 mA cm^{-2}	[20]
FeNi Foam	65 %wt.	Hydrothermal treatment and galvanic replacement reaction	72	195 at 100 mA cm^{-2}	[61]
Fe	100 %	Electrodeposited Fe	66	430 at 100 mA cm^{-2}	[26]

1

3.3 Characteristic of the anodic films obtained on high Ni content alloys: As mentioned above, a low OER activity was obtained for the 78-permalloy because of the formation of a thin coating. In order to improve the OER activity and to elucidate the effect of the anodic characteristics on the OER activity, the 78-permalloy was anodized at a potential of 50 V in ethylene glycol containing 0.08 M NH_4F and 0.02 M H_2O and its behavior was compared with that of pure Ni. From surface and cross-section SEM images, the formation of a dense layer is evidenced both in 78-permalloy and pure Ni (Figure 7). The coating thickness after anodizing was approximately 416 nm with a higher amount of F (55.5 %atm) incorporated from the electrolyte (Table 2). A thin coating was observed in pure Ni (~96 nm), highlighting the low growth kinetic in high-Ni-containing alloys. The potential cycling shows a low OER after anodizing, but the OER activity is enhanced after the potential cycling (Figure 8), as observed in the 78-permalloy anodized at 10 V (Fig. S12a). These results suggest that coatings with a high R_{ct} require a higher number of cycles to achieve optimal OER activation (see Table S2). A larger number of cycles were evaluated to determine the progress of OER activation. After 500 CV cycles, a higher OER activation is observed for the 78-permalloy, where the overpotential required to achieve a current density of 10 mA cm^{-2} is reduced to 277 mV (Table 5). Noticeable changes in OER performance are observed during the first 100 cycles, with low variation in the following 500 cycles. The Ni^{+2}/Ni^{+3} peak area increases with every cycle without a significant shift in potential during the potential cycling. The potential shift of the Ni^{+2}/Ni^{+3} peak during potential cycling is associated with Fe-doping of the Ni oxyhydroxide [13]; therefore, the increased peak area with the potential cycling in the 78-permalloy and pure Ni is primarily attributed to the increase in the number of active sites facilitated by fluoride ion leaching. The increased active sites enhance the OER activity, as

observed in the 78-permalloy anodized at 50 V, with an OER overpotential of 277 mV at 10 mA cm^{-2} (See Fig. 5). Nonetheless, Fe and Co play an important role in enhancing the OER activity of ɣ-NiOOH:Fe, which explains the best OER performance of Kovar alloy compared to 78-permalloy, even when both alloys have similar standardized currents after anodization (see Tables 3 and 5). After potential cycling, the SEM surface image shows the formation of a porous structure in the 78-permalloy due to the leaching of fluorine during the OER (Fig. 9), as was confirmed by EDS (see Table 2).

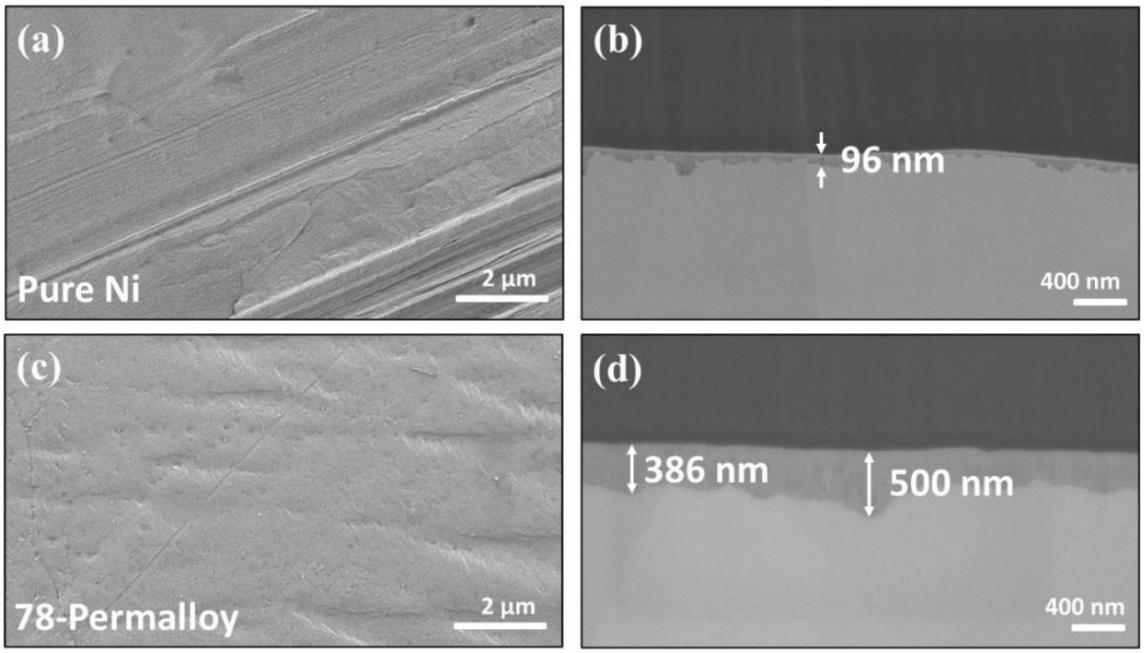


Figure 7. Surface SEM images (a, c) and cross-section SEM images (b, d) of the anodic coating obtained at 50 V in ethylene glycol containing 0.08 M NH_4F and 0.02 M H_2O in (a, b) pure Ni and (c, d) 78-permalloy.

Table 5. Electrochemical characteristics in 1M KOH of the anodic coatings obtained at 50 V in ethylene glycol containing 0.08 M NH_4F and 0.02 M H_2O.

Alloy	Overpotential[1] (mV)	Tafel slope (b/mV)	ECSA[2] (mF/cm^2)	Standardized[3] Current (mA/F)
Ni	317.2	60.78	24.5	755.7
78 Permalloy	277.1	46.48	48.7	1014.4

[1] *The OER overpotential required to achieve a current density of 10 mA* cm^{-2}.

[2] *ECSA was assessed as mentioned in section 2.5 and results are shown in Figure S7.*

[3] *Standardization of the current for OER at 1.53 V vs RHE.*

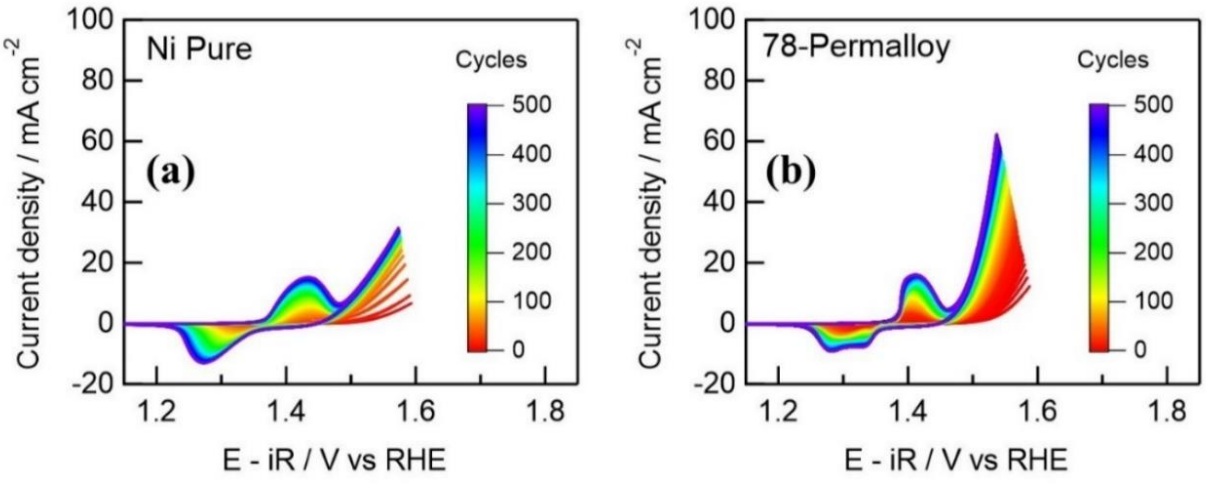


Figure 8. Potential cycling (CV) in 1 M KOH of the anodic coatings obtained at 50 V in ethylene glycol containing 0.08 M NH_4F and 0.02 M H_2O in (a) pure Ni and (b) 78-permalloy during 500 cycles.

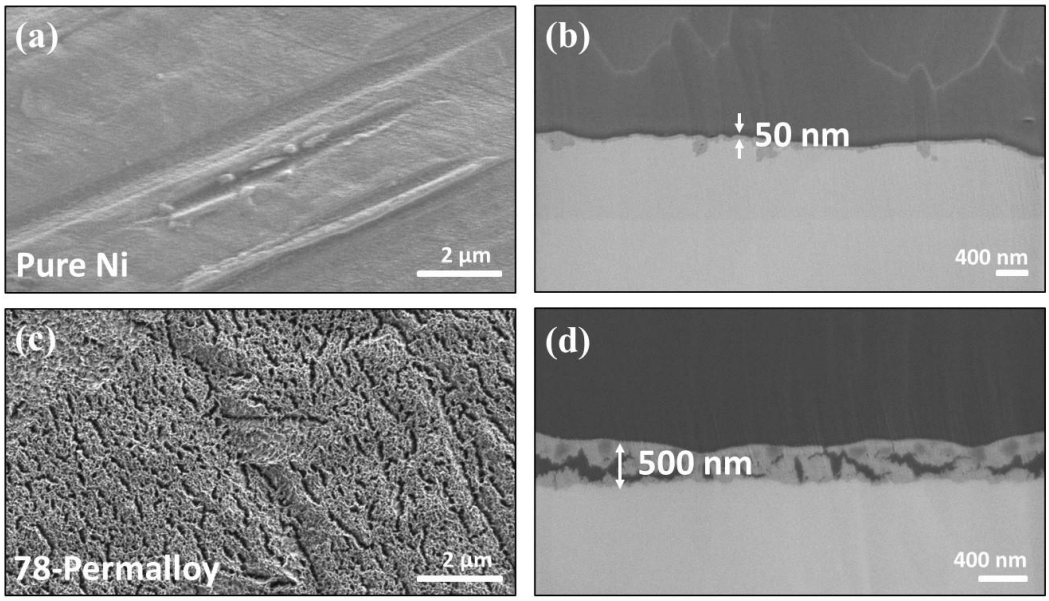


Figure 9. Surface SEM images (a, c) and cross-section SEM images (b, d) of the anodic coating after OER evaluation in 1M KOH at 293 K in (a, b) Pure Ni and (c, d) 78-permalloy.

3.4. OER/HER behavior and durability test at practical conditions: The severe chemical conditions seen in alkaline electrolyzers highlight the importance and relevance of electrode durability. Investigating the performance of anodized electrodes in practical settings is crucial to providing an understanding of the essential variables required for the development of durable and efficient electrodes [69]. OER and HER performance was assessed in 7 M KOH at 343 K, and results are summarized in Figs. S14-S16 and Table 6. The potential cycling was performed during 15 cycles and the last cycle is shown in Fig. 10. The five commercial alloys have a ~200 mV overpotential at a specific current density of 100 mA cm^{-2}, with current densities exceeding 600 mA cm^{-2} at a potential of 1.5 V (vs. RHE), which are the conditions required in alkaline electrolyzers, demonstrating a high OER catalytic activity for the anodized electrodes on FeNi and FeNiCo alloys. In addition, important facts are

evidenced after OER evaluation at 7 M KOH at 343 K. The direct use of the NiFe and NiFeCo alloys is not enough to achieve the minimal requirements in alkaline electrolyzers. The anodizing process improves the catalytic activity of the FeNi and FeNiCo alloys with a similar performance in a 7 M KOH solution at 343 K (See Fig. 10). The temperature accelerates the in-situ activation required in the 78-permalloy at 293 K (Fig. 8b). When the KOH concentration and temperature (343 K) are increased, the maximum performance is reached from the initial cycle as in the other FeNi and FeNiCo alloys (See Fig. S15). The OER performance at 343 K evidences a slight increase of the overpotential with every cycle in the anodized electrodes. Raman spectroscopy after the evaluation in 7 M KOH (Fig. S17) evidences that the characteristic peak at 474 cm^{-1} has a higher intensity than the peak at 554 cm^{-1}, especially for the Kovar alloy, which is related to the formation of γ-NiOOH with a lower amount of Fe incorporated in its structure [20]. The OER activity of the γ-NiOOH phase depends on the amount of Fe incorporated in its structure [15]. The above could explain the decrease in the OER activity with every cycle; nonetheless, further studies are required to understand the mechanisms during in-situ activation at high temperatures and high KOH concentrations. Surface SEM images after OER evaluation at 343 K reveal the dissolution process of the anodic coatings by the oxidizing and harsh environment of the alkaline electrolyzers. Less degradation is observed in dense Ni-rich coatings (Ni and 78-Permalloy) compared to the porous Fe-rich coatings (45-Permalloy, Kovar, 42Invar and super invar) (See Fig. 11). The above was confirmed by cross-sectional scanning electron microscopy (SEM) images after measuring OER at 343 K. In the case of 78-permalloy, the coating thickness varies slightly, and cracks form within the coating (Fig. 12a-b). In contrast, alloys with a higher Fe content, such as Kovar and 42-Invar, showed a significant decrease in

coating thickness, resulting in remaining film thicknesses of 480 nm and 30 nm, respectively (Figs. 12d, f). Fe has a lower stability than Ni at high pH [70,71], which could explain the higher dissolution observed in the alloys with high content of Fe (54 - 59 %wt. Fe) regarding the high Ni-content alloys (78-Permalloy and Ni). The HER performance of the anodized electrodes obtained on FeNi and FeNiCo alloys was assessed. Differences in the HER activity was observed in the anodized electrodes, with the highest HER activity for pure Ni. The increase in the Fe content in the alloy showed a limiting effect on HER activity in this study (see Table 6). Nonetheless, anodizing enhanced HER activity, which is especially remarkable for the pure Ni (Fig. S16). The above confirms the importance of nickel in HER activity in practical conditions at 7 M KOH at 343 K.

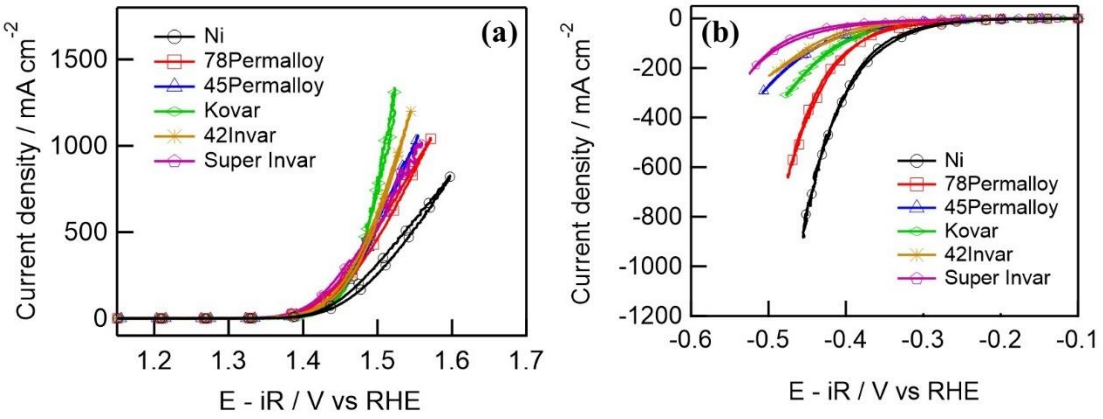


Figure 10. The 15th CV cycle in 7 M KOH at 343 K of the anodic coatings obtained on the FeNi and FeNiCo alloys under (a) OER evaluation and (b) HER evaluation. Note: Ni and 78-Permalloy were anodized at 50 V in ethylene glycol containing 0.08 M NH_4F and 0.02 M H_2O.

Table 6. Electrochemical characteristics of the anodic coatings obtained on the FeNi and FeNiCo alloys after OER evaluation in 7 M KOH at 343 K.

Alloy	Anodizing potential (V)	OER Overpotential (mV)	HER Overpotential (mV)
Ni[1]	50 V	226.6	341.8
78 Permalloy[1]	50 V	200.2	383.1
45 Permalloy[2]	10 V	206.4	426.9
Kovar[2]	10 V	214.1	404.8
42 Invar[2]	10 V	206.2	437.5
Super Invar[2]	10 V	189.0	483.2

[1] The anodizing solution is ethylene glycol containing 0.08 M NH_4F and 0.02 M H_2O.

[2] The anodizing solution is ethylene glycol containing 0.54 M NH_4F and 2.5 M H_2O.

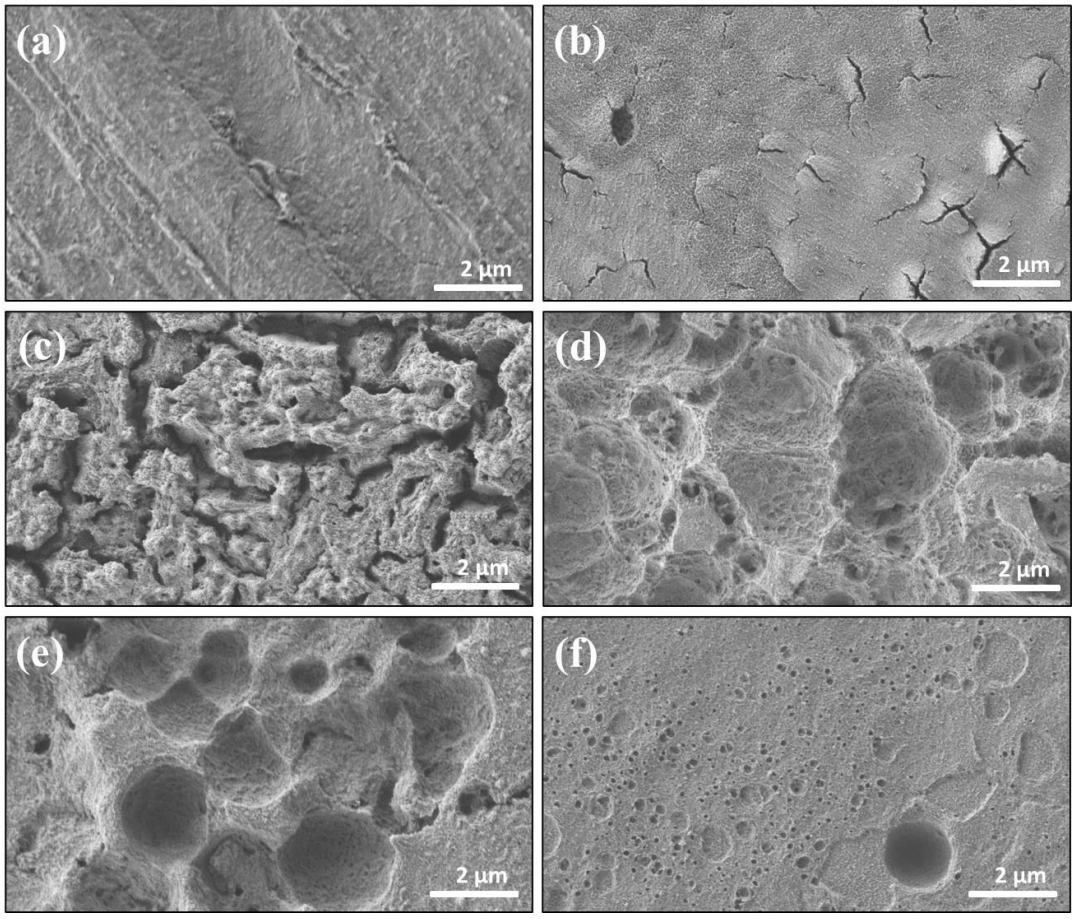


Figure 11. Surface SEM images after OER evaluation in 7 M KOH at 343 K of the anodic coatings in (a) Pure Ni, (b) 78 Permalloy, (c) 45 Permalloy, (d) Kovar, (e) 42 Invar and (f) Super Invar. Note: Ni and 78-Permalloy were anodized at 50 V in ethylene glycol containing 0.08 M NH_4F and 0.02 M H_2O.

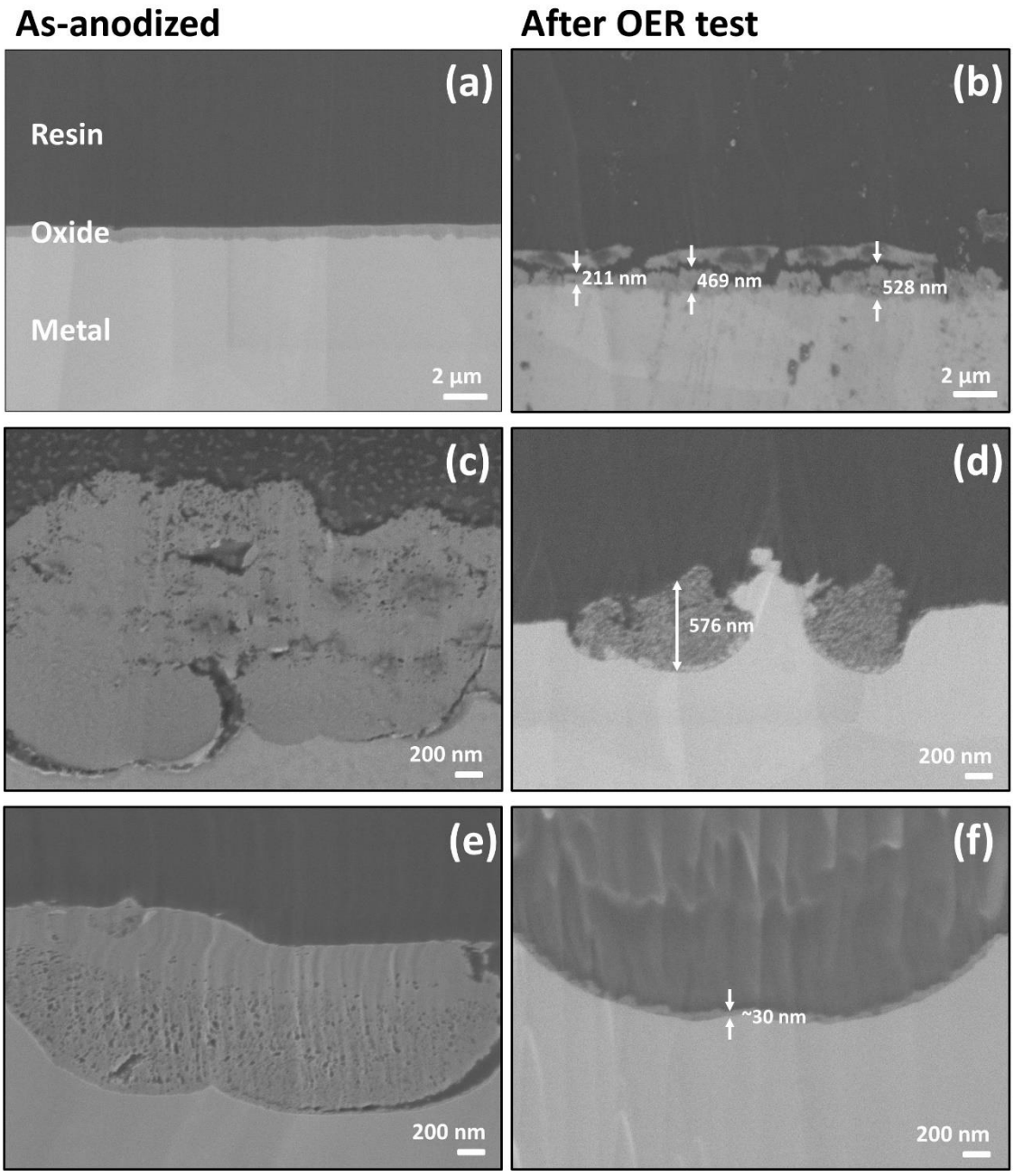


Figure 12. Cross-section images of anodized electrodes (a, c, e) and after OER test (b, d, f) in 7 M KOH at 343K in (a, b) 78-Permalloy, (c, d) Kovar and (e, f) 42 Invar. Note: 78-Permalloy was anodized at 50 V in ethylene glycol containing 0.08 M NH_4F and 0.02 M H_2O.

The durability test performed at a current density of 600 mA cm^{-2} demonstrates good catalytic activity of the anodized electrodes. During 80 h of galvanostatic electrolysis, the potential in the anodized electrodes (Fig. 13b) was lower than the substrate level, especially the Kovar and 78-permalloy (Fig. 13a). 78-permalloy and Kovar alloys showed comparable behavior during 80 h of electrolysis without significant differences in the potential with time. In both coatings the formation of γ-NiOOH:Fe was evidenced by Raman spectroscopy after the durability test, while in 42-Invar alloy low intense peaks related to the γ-NiOOH:Fe were observed, which could be related to the thin coating remained and its higher rate of dissolution (Fig. 12). The phase γ-NiOOH:Fe is highly active for OER, which explains the better performance of the 78-permalloy and Kovar alloys. In addition, Raman spectroscopy examination did not reveal the additional shoulder observed at 293 K associated with Fe_3O_4 or ɣ-FeOOH at about 685 cm^{-1} (Fig. S17).

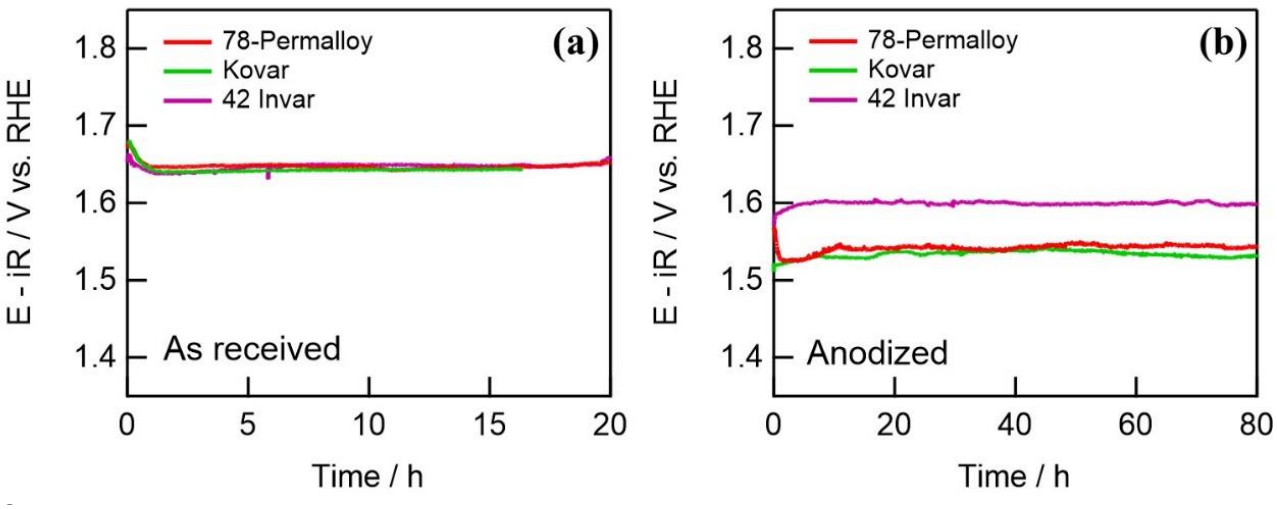


Figure 13. Constant current electrolysis of 600 mA cm^{-2} in 7 M KOH at 343K in the (a) substrates and (b) anodized electrodes. Note: 78-Permalloy was anodized at 50 V in ethylene glycol containing 0.08 M NH_4F and 0.02 M H_2O.

4. Conclusions

Anodizing FeNi and FeNiCo practical alloys produce metal fluoride coatings, which are suitable precursors to form active OER compounds. High ECSA was an important parameter to achieve a good OER activity as was observed for the Kovar alloy. During OER activation, the formation of active OER species ($Ni_xFe_{1-x}OOH$) was confirmed by Raman-spectroscopy. High-Ni content alloys generate dense coatings while porous coatings are formed in alloys with a higher amount of Fe. A low amount of Fe is not suitable for the formation of high OER active species as was observed for the 78-Permalloy.

The OER activity was improved for the 78-permalloy by anodization at a higher potential due to the formation of a higher number of active sites. The number of active sites can be controlled by changing the anodizing parameters which results in an enhancement of the OER activity. The formation of a dense layer requires an in-situ activation at 293 K with a higher number of CV cycles than the activation process observed in porous coatings (45-permalloy, Kovar, 42-Invar and Super invar).

The evaluation of the anodic coatings under practical conditions showed that the anodizing process improves the activity of OER and HER and the anodic coatings obtained are suitable to electrocatalyst the OER reaction with similar behavior in a 7 M KOH solution at 343 K. Pure Ni anodized is the most suitable electrode for the HER reaction and the activity is affected by increasing the amount of Fe in the alloy. The 78-permalloy with F-enriched showed the best performance in the durability test since the coating showed less degradation after the durability test in comparison to the high dissolution of the coating observed in Kovar and 42-Invar.

Supporting information

Experimental: Graphical illustrations of the experimental configuration for EIS and the durability test are shown in the supporting information (Figs. S1, S2 and S9). The EIS analysis was assessed by fitting the experimental results using an equivalent circuit and details and results are shown in Figs. S3-S4 and Tables S1-S2. The electrochemical active surface area results obtained by CV are summarized in Figs. S5-S8.

Results: The OER/HER performance was assessed by CV during 15 cycles. The CV curves for the 15 cycles are shown in the supporting information after the evaluation in 1 M KOH at 293 K (Fig. S12) and 7 M KOH at 343 K (Figs. S14-S16). In addition, SEM surface images of the electrodes as received condition (Fig. S10) and after OER evaluation in 1 M KOH at 293 K (Fig. S13) are observed in the supporting information. Finally, Raman spectra after the durability test are observed in Fig. S17.

Acknowledgments

This study was supported in part by the MEXT-Program for Creation of Innovative Core Technology for Power Electronics. Part of this work was conducted at Hokkaido University, supported by the Nanotechnology Platform Program of the Ministry of Education, Culture, Sports, Science and Technology (MEXT), Japan Grant Numbers JPJ009777 and A-21-HK-0036.

References

[1] A.B. Stambouli, E. Traversa, Fuel cells, an alternative to standard sources of energy, Renewable and Sustainable Energy Reviews 6 (2002) 295–304.

[2] E. Rivard, M. Trudeau, K. Zaghib, Hydrogen storage for mobility: A review, Materials 12 (2019) 1973.

[3] S. Dunn, Hydrogen futures: toward a sustainable energy system, Int J Hydrogen Energy 27 (2002) 235–264.

[4] S. Shiva Kumar, H. Lim, An overview of water electrolysis technologies for green hydrogen production, Energy Reports 8 (2022) 13793–13813. https://doi.org/https://doi.org/10.1016/j.egyr.2022.10.127.

[5] H. Schäfer, M. Chatenet, Steel: the resurrection of a forgotten water-splitting catalyst, ACS Energy Lett 3 (2018) 574–591.

[6] H. Schäfer, S. Sadaf, L. Walder, K. Kuepper, S. Dinklage, J. Wollschläger, L. Schneider, M. Steinhart, J. Hardege, D. Daum, Stainless steel made to rust: a robust water-splitting catalyst with benchmark characteristics, Energy Environ Sci 8 (2015) 2685–2697.

[7] S. Teske, Achieving the Paris climate agreement goals: Global and regional 100% renewable energy scenarios with non-energy GHG pathways for+ 1.5 C and+ 2 C, Springer Nature, 2019.

[8] E.T. Commission, Making Mission Possible Delivering a Net-Zero Economy. 2020, Sept Ww W Energy-Transit Orgpublicationsmaking-Mission-Possible Download-Form (n.d.).

[9] B.H.R. Suryanto, Y. Wang, R.K. Hocking, W. Adamson, C. Zhao, Overall electrochemical splitting of water at the heterogeneous interface of nickel and iron oxide, Nat Commun 10 (2019) 5599.

[10] M. Chatenet, B.G. Pollet, D.R. Dekel, F. Dionigi, J. Deseure, P. Millet, R.D. Braatz, M.Z. Bazant, M. Eikerling, I. Staffell, Water electrolysis: from textbook knowledge to the latest scientific strategies and industrial developments, Chem Soc Rev 51 (2022) 4583–4762.

[11] R. Tomizawa, C. Zhu, E. Tsuji, Y. Aoki, H. Habazaki, Formation of Nanoporous NiFe2O4 Oxide Films by Anodizing of Fe-Ni Alloy, ECS Trans 75 (2017) 67.

[12] F. Ganci, T. Baguet, G. Aiello, V. Cusumano, P. Mandin, C. Sunseri, R. Inguanta, Nanostructured Ni based anode and cathode for alkaline water electrolyzers, Energies (Basel) 12 (2019) 3669.

[13] L. Trotochaud, S.L. Young, J.K. Ranney, S.W. Boettcher, Nickel–iron oxyhydroxide oxygen-evolution electrocatalysts: the role of intentional and incidental iron incorporation, J Am Chem Soc 136 (2014) 6744–6753.

[14] S. Klaus, Y. Cai, M.W. Louie, L. Trotochaud, A.T. Bell, Effects of Fe electrolyte impurities on Ni (OH) 2/NiOOH structure and oxygen evolution activity, The Journal of Physical Chemistry C 119 (2015) 7243–7254.

[15] S. Anantharaj, S. Kundu, S. Noda, "The Fe Effect": A review unveiling the critical roles of Fe in enhancing OER activity of Ni and Co based catalysts, Nano Energy 80 (2021) 105514.

[16] M. Vandichel, K. Laasonen, I. Kondov, Oxygen evolution and reduction on Fe-doped NiOOH: Influence of solvent, dopant position and reaction mechanism, Top Catal 63 (2020) 833–845.

[17] J. Zaffran, M.B. Stevens, C.D.M. Trang, M. Nagli, M. Shehadeh, S.W. Boettcher, M. Caspary Toroker, Influence of electrolyte cations on Ni (Fe) OOH catalyzed oxygen evolution reaction, Chemistry of Materials 29 (2017) 4761–4767.

[18] D. Friebel, M.W. Louie, M. Bajdich, K.E. Sanwald, Y. Cai, A.M. Wise, M.-J. Cheng, D. Sokaras, T.-C. Weng, R. Alonso-Mori, Identification of highly active Fe sites in (Ni, Fe) OOH for electrocatalytic water splitting, J Am Chem Soc 137 (2015) 1305–1313.

[19] N. Yamada, S. Kitano, Y. Yato, D. Kowalski, Y. Aoki, H. Habazaki, In Situ Activation of Anodized Ni–Fe Alloys for the Oxygen Evolution Reaction in Alkaline Media, ACS Appl Energy Mater (2020).

[20] M.W. Louie, A.T. Bell, An investigation of thin-film Ni–Fe oxide catalysts for the electrochemical evolution of oxygen, J Am Chem Soc 135 (2013) 12329–12337.

[21] D.A. Corrigan, The catalysis of the oxygen evolution reaction by iron impurities in thin film nickel oxide electrodes, J Electrochem Soc 134 (1987) 377.

[22] E. Tsuji, A. Imanishi, K. Fukui, Y. Nakato, Electrocatalytic activity of amorphous RuO2 electrode for oxygen evolution in an aqueous solution, Electrochim Acta 56 (2011) 2009–2016.

[23] B. Yang, J. Xu, D. Bin, J. Wang, J. Zhao, Y. Liu, B. Li, X. Fang, Y. Liu, L. Qiao, L. Liu, B. Liu, Amorphous phosphatized ruthenium-iron bimetallic nanoclusters with Pt-like activity for hydrogen evolution reaction, Appl Catal B 283 (2021) 119583. https://doi.org/https://doi.org/10.1016/j.apcatb.2020.119583.

[24] B.M. Hunter, J.R. Winkler, H.B. Gray, Iron is the active site in nickel/iron water oxidation electrocatalysts, Molecules 23 (2018) 903.

[25] C. Pei, Y. Gu, Z. Liu, X. Yu, L. Feng, Fluoridated iron–nickel layered double hydroxide for enhanced performance in the oxygen evolution reaction, ChemSusChem 12 (2019) 3849–3855.

[26] J.R. Swierk, S. Klaus, L. Trotochaud, A.T. Bell, T.D. Tilley, Electrochemical study of the energetics of the oxygen evolution reaction at nickel iron (oxy) hydroxide catalysts, The Journal of Physical Chemistry C 119 (2015) 19022–19029.

[27] X. Zhu, C. Tang, H.-F. Wang, B.-Q. Li, Q. Zhang, C. Li, C. Yang, F. Wei, Monolithic-structured ternary hydroxides as freestanding bifunctional electrocatalysts for overall water splitting, J Mater Chem A Mater 4 (2016) 7245–7250.

[28] H.H. Farrag, S.Y. Sayed, N.K. Allam, A.M. Mohammad, Emerging nanoporous anodized stainless steel for hydrogen production from solar water splitting, J Clean Prod 274 (2020) 122826.

[29] P. Kuang, B. Zhu, Y. Li, H. Liu, J. Yu, K. Fan, Graphdiyne: a superior carbon additive to boost the activity of water oxidation catalysts, Nanoscale Horiz 3 (2018) 317–326.

[30] Z. Zhao, H. Wu, H. He, X. Xu, Y. Jin, A High-Performance Binary Ni–Co Hydroxide-based Water Oxidation Electrode with Three-Dimensional Coaxial Nanotube Array Structure, Adv Funct Mater 24 (2014) 4698–4705.

[31] W. Wang, J. Luo, S. Chen, Carbon oxidation reactions could misguide the evaluation of carbon black-based oxygen-evolution electrocatalysts, Chemical Communications 53 (2017) 11556–11559.

[32] J. Yang, S. Park, K.Y. Choi, H.-S. Park, Y.-G. Cho, H. Ko, H.-K. Song, Activity-durability coincidence of oxygen evolution reaction in the presence of carbon corrosion: case study of MnCo2O4 spinel with carbon black, ACS Sustain Chem Eng 6 (2018) 9566–9571.

[33] H. Sun, X. Xu, Z. Yan, X. Chen, L. Jiao, F. Cheng, J. Chen, Superhydrophilic amorphous Co–B–P nanosheet electrocatalysts with Pt-like activity and durability for the hydrogen evolution reaction, J Mater Chem A Mater 6 (2018) 22062–22069.

[34] F. Ganci, B. Patella, E. Cannata, V. Cusumano, G. Aiello, C. Sunseri, P. Mandin, R. Inguanta, Ni alloy nanowires as high efficiency electrode materials for alkaline electrolysers, Int J Hydrogen Energy 46 (2021) 35777–35789. https://doi.org/https://doi.org/10.1016/j.ijhydene.2020.11.208.

[35] F. Ganci, B. Buccheri, B. Patella, E. Cannata, G. Aiello, P. Mandin, R. Inguanta, Electrodeposited nickel–zinc alloy nanostructured electrodes for alkaline electrolyzer, Int J Hydrogen Energy 47 (2022) 11302–11315. https://doi.org/https://doi.org/10.1016/j.ijhydene.2021.09.221.

[36] M. Li, H. Liu, L. Feng, Fluoridation-induced high-performance catalysts for the oxygen evolution reaction: A mini review, Electrochem Commun 122 (2021) 106901. https://doi.org/https://doi.org/10.1016/j.elecom.2020.106901.

[37] Y. Xue, Y. Wang, H. Liu, X. Yu, H. Xue, L. Feng, Electrochemical oxygen evolution reaction catalyzed by a novel nickel–cobalt-fluoride catalyst, Chemical Communications 54 (2018) 6204–6207.

[38] C. Pei, H. Chen, B. Dong, X. Yu, L. Feng, Electrochemical oxygen evolution reaction efficiently catalyzed by a novel porous iron-cobalt-fluoride nanocube easily derived from 3-dimensional Prussian blue analogue, J Power Sources 424 (2019) 131–137.

[39] J. Fan, Z. Chen, H. Shi, G. Zhao, In situ grown, self-supported iron–cobalt–nickel alloy amorphous oxide nanosheets with low overpotential toward water oxidation, Chemical Communications 52 (2016) 4290–4293.

[40] M. Nishimoto, S. Kitano, D. Kowalski, Y. Aoki, H. Habazaki, Highly Active and Durable FeNiCo Oxyhydroxide Oxygen Evolution Reaction Electrocatalysts Derived from Fluoride Precursors, ACS Sustain Chem Eng 9 (2021) 9465–9473.

[41] F. Bao, E. Kemppainen, I. Dorbandt, F. Xi, R. Bors, N. Maticiuc, R. Wenisch, R. Bagacki, C. Schary, U. Michalczik, Host, suppressor, and promoter—the roles of Ni and Fe on oxygen evolution reaction activity and stability of NiFe alloy thin films in alkaline media, ACS Catal 11 (2021) 10537–10552.

[42] A. Alobaid, C. Wang, R.A. Adomaitis, Mechanism and Kinetics of HER and OER on NiFe LDH Films in an Alkaline Electrolyte, J Electrochem Soc 165 (2018) J3395–J3404.

[43] E. Cossar, M.S.E. Houache, Z. Zhang, E.A. Baranova, Comparison of electrochemical active surface area methods for various nickel nanostructures, Journal of Electroanalytical Chemistry 870 (2020) 114246.

[44] X. Fu, T. Li, F. Qi, S. Zhang, J. Wen, W. Shu, P. Luo, R. Zhang, S. Hu, Q. Liu, Designing high electrochemical surface area between polyaniline and hydrogel polymer electrolyte for flexible supercapacitors, Appl Surf Sci 507 (2020) 145135.

[45] J.J. Kelly, The influence of fluoride ions on the passive dissolution of titanium, Electrochim Acta 24 (1979) 1273–1282. https://doi.org/https://doi.org/10.1016/0013-4686(79)87084-X.

[46] M. Nishimoto, Z. Xiong, S. Kitano, Y. Aoki, H. Habazaki, The effect of anodizing temperature on the oxygen evolution reaction activity of anodized FeNiCo alloy in alkaline electrolyte, Electrochim Acta 427 (2022) 140875. https://doi.org/https://doi.org/10.1016/j.electacta.2022.140875.

[47] D. Quintero, M.A. Gómez, W.S. Araujo, F. Echeverría, J.A. Calderón, Influence of the electrical parameters of the anodizing PEO process on wear and corrosion resistance of niobium, Surf Coat Technol 380 (2019) 125067. https://doi.org/https://doi.org/10.1016/j.surfcoat.2019.125067.

[48] K. Xie, M. Guo, H. Huang, Y. Liu, Fabrication of iron oxide nanotube arrays by electrochemical anodization, Corros Sci 88 (2014) 66–75. https://doi.org/https://doi.org/10.1016/j.corsci.2014.07.019.

[49] K.Y. Kim, R.D. Smith, O.F. Devereux, Charge Transfer Processes during Anodic Polarization of Aluminum, J Electrochem Soc 123 (1976) 1789.

[50] M. Kocabaş, C. Örnek, M. Curioni, N. Cansever, Nickel fluoride as a surface activation agent for electroless nickel coating of anodized AA1050 aluminum alloy, Surf Coat Technol 364 (2019) 231–238. https://doi.org/https://doi.org/10.1016/j.surfcoat.2019.03.003.

[51] N. Akbari, S. Nandy, K.H. Chae, M.M. Najafpour, Dynamic Changes of an Anodized FeNi Alloy during the Oxygen Evolution Reaction under Alkaline Conditions, Langmuir 39 (2023) 11807–11818. https://doi.org/10.1021/acs.langmuir.3c01540.

[52] P. Thangadurai, S. Ramasamy, R. Kesavamoorthy, Raman studies in nanocrystalline lead (II) fluoride, Journal of Physics: Condensed Matter 17 (2005) 863.

[53] H. Ullah, N. Batisse, K. Guerin, G. Rogez, P. Bonnet, Synthesis of NiF2 and NiF2·4H2O Nanoparticles by Microemulsion and Their Self-Assembly, Langmuir 36 (2020) 8461–8475.

[54] Y. Zhou, N. López, The role of Fe species on NiOOH in oxygen evolution reactions, ACS Catal 10 (2020) 6254–6261.

[55] R.N. Singh, J.P. Pandey, K.L. Anitha, Preparation of electrodeposited thin films of nickel-iron alloys on mild steel for alkaline water electrolysis. Part I: studies on oxygen evolution, Int J Hydrogen Energy 18 (1993) 467–473.

[56] Y. Yan, B.Y. Xia, B. Zhao, X. Wang, A review on noble-metal-free bifunctional heterogeneous catalysts for overall electrochemical water splitting, J Mater Chem A Mater 4 (2016) 17587–17603.

[57] S. Anantharaj, H. Sugime, S. Noda, Why shouldn't double-layer capacitance (Cdl) be always trusted to justify Faradaic electrocatalytic activity differences?, Journal of Electroanalytical Chemistry 903 (2021) 115842. https://doi.org/https://doi.org/10.1016/j.jelechem.2021.115842.

[58] D.L.A. De Faria, S. Venâncio Silva, M.T. De Oliveira, Raman microspectroscopy of some iron oxides and oxyhydroxides, Journal of Raman Spectroscopy 28 (1997) 873–878.

[59] K. Hedenstedt, J. Bäckström, E. Ahlberg, In-situ Raman spectroscopy of α-and γ-FeOOH during cathodic load, J Electrochem Soc 164 (2017) H621.

[60] C. Tang, R. Zhang, W. Lu, Z. Wang, D. Liu, S. Hao, G. Du, A.M. Asiri, X. Sun, Energy-saving electrolytic hydrogen generation: Ni2P nanoarray as a high-

performance non-noble-metal Electrocatalyst, Angewandte Chemie International Edition 56 (2017) 842–846.

[61] H. Zhang, G. Shen, X. Liu, B. Ning, C. Shi, L. Pan, X. Zhang, Z.-F. Huang, J.-J. Zou, Self-supporting NiFe LDH-MoSx integrated electrode for highly efficient water splitting at the industrial electrolysis conditions, Chinese Journal of Catalysis 42 (2021) 1732–1741.

[62] J.M. Runge, A brief history of anodizing aluminum, The Metallurgy of Anodizing Aluminum: Connecting Science to Practice (2018) 65–148.

[63] H. Yang, L. Gong, H. Wang, C. Dong, J. Wang, K. Qi, H. Liu, X. Guo, B.Y. Xia, Preparation of nickel-iron hydroxides by microorganism corrosion for efficient oxygen evolution, Nat Commun 11 (2020) 5075.

[64] W. Li, Q. Hu, Y. Liu, M. Zhang, J. Wang, X. Han, C. Zhong, W. Hu, Y. Deng, Powder metallurgy synthesis of porous Ni-Fe alloy for oxygen evolution reaction and overall water splitting, J Mater Sci Technol 37 (2020) 154–160. https://doi.org/https://doi.org/10.1016/j.jmst.2019.06.021.

[65] H. Yuan, S. Wang, X. Gu, B. Tang, J. Li, X. Wang, One-step solid-phase boronation to fabricate self-supported porous FeNiB/FeNi foam for efficient electrocatalytic oxygen evolution and overall water splitting, J Mater Chem A Mater 7 (2019) 19554–19564.

[66] Q. Yang, X. Le, L. Wenzhen, Electrocatalytic Oxygen Evolution over Supported Small Amorphous Ni–Fe Nanoparticles in Alkaline Electrolyte, (2014).

[67] Z. Yin, R. He, Y. Zhang, L. Feng, X. Wu, T. Wågberg, G. Hu, Electrochemical deposited amorphous FeNi hydroxide electrode for oxygen evolution reaction, Journal of Energy Chemistry 69 (2022) 585–592. https://doi.org/https://doi.org/10.1016/j.jechem.2022.01.020.

[68] Y. Zhang, X. Hou, X. Li, D. Li, F. Huang, Q. Wei, FeNi alloy nanoparticles embedded in electrospun nitrogen-doped carbon fibers for efficient oxygen evolution reaction, J Colloid Interface Sci 578 (2020) 805–813. https://doi.org/https://doi.org/10.1016/j.jcis.2020.06.044.

[69] N. Todoroki, T. Wadayama, Dissolution of constituent elements from various austenitic stainless steel oxygen evolution electrodes under potential cycle loadings, Int J Hydrogen Energy 47 (2022) 32753–32762. https://doi.org/https://doi.org/10.1016/j.ijhydene.2022.07.175.

[70] B. Beverskog, I. Puigdomenech, Revised Pourbaix diagrams for nickel at 25–300 °C, Corros Sci 39 (1997) 969–980. https://doi.org/https://doi.org/10.1016/S0010-938X(97)00002-4.

[71] B. Beverskog, I. Puigdomenech, Revised pourbaix diagrams for iron at 25–300 °C, Corros Sci 38 (1996) 2121–2135. https://doi.org/https://doi.org/10.1016/S0010-938X(96)00067-4.